

Switching of a Magnet by Spin-Orbit Torque from a Topological Dirac Semimetal

Jinjun Ding, Chuanpu Liu, Vijaysankar Kalappattil, Yuejie Zhang, Oleksandr Mosendz, Uppalaiah Erugu, Rui Yu, Jifa Tian, August DeMann, Stuart B. Field, Xiaofei Yang, Haifeng Ding, Jinke Tang, Bruce Terris, Albert Fert, Hua Chen, and Mingzhong Wu*

Recent experiments show that topological surface states (TSS) in topological insulators (TI) can be exploited to manipulate magnetic ordering in ferromagnets. In principle, TSS should also exist for other topological materials, but it remains unexplored as to whether such states can also be utilized to manipulate ferromagnets. Herein, current-induced magnetization switching enabled by TSS in a non-TI topological material, namely, a topological Dirac semimetal α -Sn, is reported. The experiments use an α -Sn/Ag/CoFeB trilayer structure. The magnetization in the CoFeB layer can be switched by a charge current at room temperature, without an external magnetic field. The data show that the switching is driven by the TSS of the α -Sn layer, rather than spin-orbit coupling in the bulk of the α -Sn layer or current-produced heating. The switching efficiency is as high as in TI systems. This shows that the topological Dirac semimetal α -Sn is as promising as TI materials in terms of spintronic applications.

Spin-orbit torque (SOT) refers to a torque exerted on magnetic moments in a magnet by a spin current in a neighboring material that is produced by a charge current via spin-orbit coupling (SOC). The SOT phenomenon is of major fundamental and practical interest. Through SOT processes, one can use electric currents to manipulate magnetic ordering, and such manipulation is of great technological significance.

Earlier work has focused on layered heterostructures based on heavy metals, such as Pt, Ta, and W.^[1,2,3] Strong SOC in heavy metals has allowed for experimental demonstrations of SOT-driven magnetization reversal,^[1,2,3] domain wall motion,^[4]

and magnetization precession.^[5] Such demonstrations have fueled considerable ongoing efforts in the development of SOT-based energy-efficient spintronic devices, including memory, logic, and microwave and terahertz oscillators.

Very recent work, however, shows that SOT devices with even higher efficiency may be achievable if one replaces the heavy metal with a topological insulator (TI). Due to intrinsic spin-momentum locking of the topological surface states (TSS), a TI material can convert a charge current into a spin current at an efficiency that is substantially higher than in a heavy metal. In particular, highly efficient magnetization switching has already been realized in a large number of TI/magnet bilayered systems.^[6,7,8,9,10,11,12,13] The TI


component has ranged from Bi₂Se₃ to (Bi_{1-x}Sb_x)₂Te₃ to Bi_{0.9}Sb_{0.1} to SmB₆. The magnetic layers have included ferromagnetic metals, ferrimagnetic alloys, ferrimagnetic insulators, and magnetically doped TI films.

In principle, topological surface states (TSS) should exist in any topological quantum material, including Dirac semimetals and Weyl semimetals. Whenever a topological material is interfaced with a topologically trivial material, TSS arise naturally at the interface, as a result of different band topologies of the two materials. These TSS are all expected to exhibit spin-momentum locking, due to the broken inversion symmetry at the interface.

Dr. J. Ding, Dr. C. Liu, Dr. V. Kalappattil, Y. Zhang, Dr. R. Yu, A. DeMann, Prof. S. B. Field, Prof. H. Chen, Prof. M. Wu
 Department of Physics
 Colorado State University
 Fort Collins, CO 80523, USA
 E-mail: mww@colostate.edu

Y. Zhang, Prof. X. Yang
 School of Optical and Electronic Information
 Huazhong University of Science and Technology
 Wuhan, Hubei 430074, China

Dr. O. Mosendz, Dr. B. Terris
 Western Digital Research Center
 Western Digital Corporation
 San Jose, CA 95119, USA

 The ORCID identification number(s) for the author(s) of this article can be found under <https://doi.org/10.1002/adma.202005909>.

U. Erugu, Prof. J. Tian, Prof. J. Tang
 Department of Physics and Astronomy
 University of Wyoming
 Laramie, WY 82071, USA

Dr. R. Yu, Prof. H. Ding
 National Laboratory of Solid State Microstructures
 and Department of Physics
 Nanjing University
 Nanjing, Jiangsu 210093, China

Prof. A. Fert
 Unité Mixte de Physique, CNRS, Thales
 Université Paris-Saclay
 Palaiseau 91767, France

Prof. H. Chen
 School of Advanced Materials Discovery
 Colorado State University
 Fort Collins, CO 80523, USA

DOI: 10.1002/adma.202005909

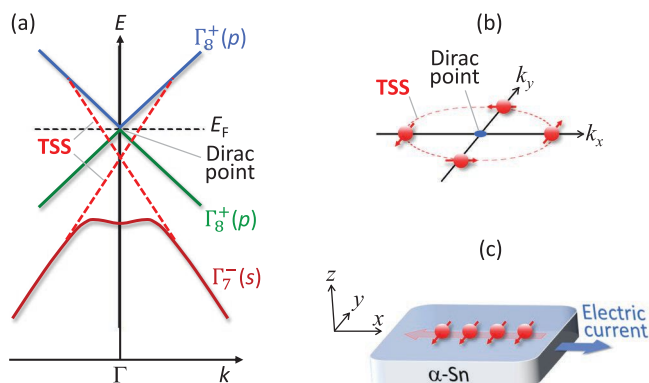


Figure 1. Schematic of the band structure and topological surface states (TSS) in Dirac semimetal α -Sn thin films. a) Band structure. b) Spin-momentum locking of the TSS at the Fermi level (E_F). c) Spin current on an α -Sn surface.

As such, one would naturally expect that non-TI topological materials may have a charge-to-spin conversion efficiency as high as in TI systems and therefore may also be used to effectively manipulate magnets. Such a possibility has been demonstrated very recently for Weyl semimetals, by the use of $\text{WTe}_2/\text{Ni}_{81}\text{Fe}_{19}$ bilayered structures.^[14] WTe_2 is a topological Weyl semimetal, a non-TI material.^[14,15,16,17] As of yet, no work has been reported for topological Dirac semimetals.

This article reports on the experimental observation of highly efficient magnetization switching enabled by SOT from a non-TI topological quantum material, namely, the topological Dirac semimetal α -Sn. Unstrained α -Sn is a gapless semiconductor in which the quadratic conduction and valence bands touch at the Γ point near the Fermi level. This band touching is protected by the cubic symmetry of the α -Sn structure. If the cubic symmetry is broken by a tensile strain along the [001] or [111] directions, the two bands cross each other near the Fermi level, forming two Dirac points. This gives rise to a topological Dirac semimetal (TDS) phase.^[18,19,20] Such band crossing is protected by the rotational symmetry that remains unbroken by the tensile strain.

The origin of the TSS in the strain driven TDS α -Sn film of interest here comes from band inversion. **Figure 1** elucidates the band configuration. The conduction and valence (Γ_8^+) bands near the Fermi level are derived from p electrons, while the s electron-derived (Γ_7^-) band is below the Fermi level, as shown in Figure 1a. This band structure is quite different from that for other group-IV diamond structure semiconductors such as Si and Ge. Note that the Γ_7^- band is pushed below the Fermi level. This is mainly due to the scalar relativistic effects that affect the s electrons.^[21,22] The TSS bridge the Γ_8^+ conduction band and the Γ_7^- valence band,^[18,19] as indicated by the red dashed lines in Figure 1a. Figure 1b conveys the essence of the spin-momentum locking of the electrons for the TSS in α -Sn. This locking has been previously confirmed via spin-resolved, angle-resolved photoemission spectroscopy (ARPES).^[23,24] Figure 1c conveys the potential for efficient charge-to-spin conversion that has been previously demonstrated via spin pumping experiments by Rojas-Sanchez et al.^[25] Note that such TSS are different from topological Fermi arc states; Fermi arc states may also be present in α -Sn thin films but they do not contribute to the switching, as discussed shortly.

In this work, α -Sn thin films were grown on single-crystal Si substrates by sputtering. The lattice constant of α -Sn ($a = 6.489 \text{ \AA}$) is larger than that of Si ($a = 5.4307 \text{ \AA}$); this lattice mismatch gives rise to a perpendicular tensile strain in the α -Sn films and therefore makes the films a TDS (topological Dirac semimetal) phase.^[18,19,20] The TDS properties of the α -Sn films were characterized through electrical transport measurements and analyses. The switching experiment was carried out with a micron-sized rectangular element made of an α -Sn(6 nm)/Ag(2 nm)/CoFeB(2 nm) trilayered structure. The magnetization in CoFeB favors alignment along the length directions of the rectangular element. Field-free, current-induced switching of the magnetization between the length directions was observed at room temperature, with a switching current density (J_c) of about $1.7 \times 10^6 \text{ A cm}^{-2}$. The analysis based on J_c yielded an SOT efficiency of 6.1 in the α -Sn film. This SOT efficiency is comparable to that for TI systems and is substantially higher than that for heavy metals. Control measurements indicate that the switching is enabled mostly by the TSS in the α -Sn film, rather than by SOC in the bulk of the α -Sn film or current-produced heating effects in the structure.

Three important points should be highlighted prior to the presentation of the results. (1) The TDS is a relatively newly-discovered topological quantum phase. In comparison with other TDS materials,^[26,27,28] α -Sn is more attractive because: (a) it is a single-element material and is therefore relatively easy to grow and (b) it can transform to other topological phases, such as a TI or a topological Weyl semimetal, under certain strain or magnetic field conditions.^[18,19,20] (2) This work, together with the recent work on Weyl semimetals,^[14] demonstrate that non-TI topological quantum materials may be as promising as TI materials in terms of spintronics applications. This significantly broadens the range of SOT materials available for the highly-efficient manipulation of magnetism. (3) These results will likely have a transformative impact on the ongoing industrial development of SOT devices. There are three reasons: (a) The α -Sn thin films were grown on Si, a common industrial substrate. (b) They were grown by sputtering, an industry-friendly film growth technique. (c) Highly-efficient switching was demonstrated at room temperature without any external magnetic field.

The α -Sn films were grown on commercial single-crystal (111) Si substrates by DC sputtering, as described in detail in Section S1, Supporting Information. The representative structural and morphological properties of the films are presented in **Figure 2**. Figure 2a shows X-ray diffraction (XRD) spectra for a 5.8 nm-thick Sn film (blue) and a 9.6 nm-thick Sn film (green). Figure 2b shows the XRD (111) fitting results for the 5.8 nm film. The red profile shows the fit to a Voigt trial function, the red vertical dashed line shows the peak position of the Voigt profile, and the gray vertical dashed line shows the theoretically expected position of the peak. Figures 2c and 2d present an atomic force microscopy (AFM) surface image in 2D and 3D forms, respectively, for the 5.8 nm film. The roughness value indicated was determined by averaging over the AFM measurements on five different $1 \mu\text{m} \times 1 \mu\text{m}$ areas; the indicated uncertainty corresponds to the standard deviation.

Four results are evident from the data in Figure 2. (1) In Figure 2a, the 5.8 nm film shows a peak for α -Sn and no peaks for β -Sn, while the 9.6 nm film shows a peak for β -Sn and no

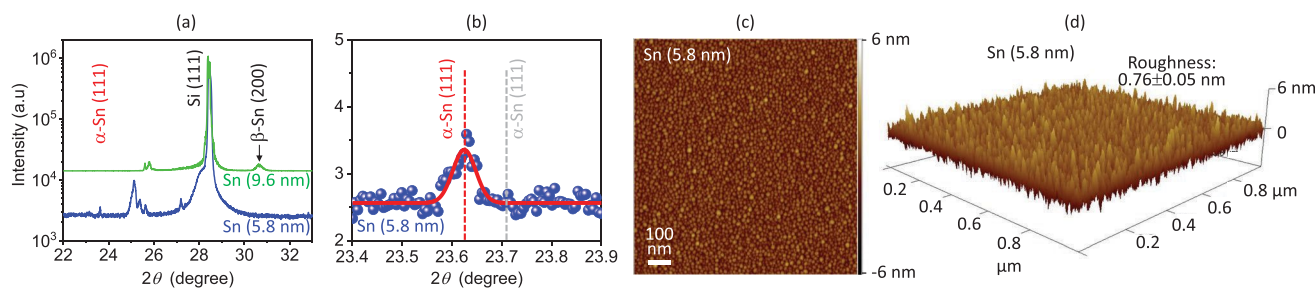


Figure 2. Structural and morphological properties of α -Sn thin films. a) XRD spectra of a 5.8 nm-thick Sn film and a 9.6 nm-thick Sn film. b) Fitting of the α -Sn (111) peak of the 5.8 nm film. c) AFM surface image of the 5.8 nm film. d) 3D form of the image in (c).

peaks for α -Sn. This shows that the thinner 5.8 nm film is α -Sn while the thicker 9.6 nm film is β -Sn. This phase change with thickness is considered in Section S2, Supporting Information.

(2) Note that there is only one peak for the α -Sn in the 5.8 nm film. This is a possible indication of quasi-epitaxial growth of the α -Sn film.

(3) The α -Sn (111) peak in Figure 2b appears on the left side of the theoretically expected peak position. This indicates the presence of a perpendicular tensile strain or an in-plane compressive strain in the film. This is consistent with the expectation that an α -Sn film grown on a Si substrate should exhibit an in-plane compressive strain because the lattice constant of α -Sn is larger than that of Si. The fitting in Figure 2b yields a lattice constant of about 6.514 Å for the 5.8 nm film. This corresponds to a perpendicular tensile strain of $\approx 0.38\%$. It is this significant strain that makes the α -Sn film a topological Dirac semimetal (TDS).^[18,19,20]

(4) Figures 2c and 2d show that the 5.8 nm film has low roughness. This, in turn, can facilitate the fabrication of layered heterostructures with high-quality interfaces for switching

experiments. It is noteworthy that the surface morphology of the α -Sn film is very similar to that of α -Sn films grown previously by molecular beam epitaxy (MBE).^[29] Figure 2c indicates an α -Sn grain size in the 15–20 nm range, which is comparable to the range of grain sizes for MBE-grown films.^[29]

Figure 3 presents transport data that show the features of TDS materials. Figure 3a depicts the basic measurement configuration. Figure 3b gives the Hall resistance (R_{xy}) and longitudinal resistance (R_{xx}) of a Hall bar structure made of a Si/ α -Sn(6.0 nm)/Si₃N₄(3 nm) sample versus the applied perpendicular magnetic field (H) at room temperature. Figures 3d and 3e show R_{xx} and the corresponding conductance (G_{xx}) data, respectively, for a Si/ α -Sn(5.8 nm)/SiO₂(1 nm) sample measured as a function of temperature (T) at $H = 0$.

The data in Figure 3b show three important results. (1) The R_{xy} versus H response is strongly nonlinear, as shown by the black circles. This strongly suggests the presence of parallel conduction channels in the α -Sn film, something that is fairly common in TDS materials.^[30] In contrast, the thicker β -Sn films exhibit the usual linear R_{xy} versus H responses, as shown

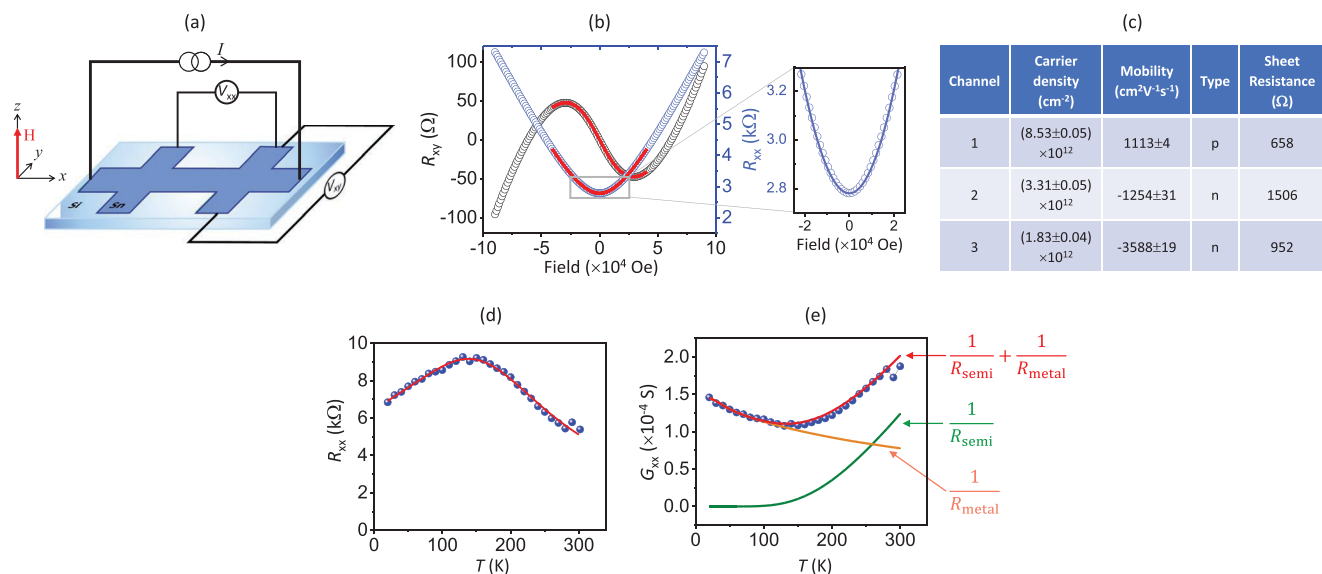


Figure 3. Electrical transport properties of α -Sn thin films. a) Measurement configuration. b) Hall resistance (R_{xy} , left axis) and longitudinal resistance (R_{xx} , right axis) of a Si/ α -Sn(6 nm)/Si₃N₄(3 nm) sample measured as a function of the magnetic field (H). The circles show the experimental data, while the curves show numerical fits. c) Carrier properties obtained from the numerical fitting shown in (b). d) R_{xx} of a Si/ α -Sn(5.8 nm)/SiO₂(1 nm) sample measured as a function of temperature (T) at $H = 0$. e) Corresponding longitudinal conductance (G_{xx}) of R_{xx} in (d). In (d,e), the solid circles show the experimental data, while the curves are numerical fits.

in Figure S4, Supporting Information. (2) The R_{xx} versus H data show a quadratic field dependence at low fields ($H < 20$ kOe), as indicated by the quadratic fit (blue curve) in the right graph in Figure 3b. This quadratic response is common for non-magnetic systems, including TDS materials,^[27,30] and is believed to arise from the Lorentz deflection of the carriers in the α -Sn film. (3) The R_{xx} versus H data show non-saturating linear magnetoresistance at high fields ($H > 50$ kOe). This is an important property of TDS materials, although its physical origin is still under debate.^[27,30,31]

The above three results, taken together, clearly indicate that the 6.0 nm Sn film is a semimetal, rather than a metal. In other words, the film is α -Sn, rather than β -Sn. This conclusion is further supported by the fact that the resistivity of these α -Sn films ($5.6 \times 10^{-4} \Omega \text{ cm}$) is more than one order of magnitude higher than for metallic β -Sn films grown on Si substrates ($1.5 \times 10^{-5} \Omega \text{ cm}$). These results, together with the strain property indicated by the XRD data in Figure 2b, suggest that the 6.0 nm film is a topological Dirac semimetal.

In addition to the above qualitative results, one can also achieve a more quantitative understanding on the properties of the α -Sn films by numerically fitting the $R_{xx}(H)$ and $R_{xy}(H)$ data in Figure 3b, as in previous works.^[30,32,33] The two red curves in Figure 3b show the simultaneous fits of $R_{xx}(H)$ and $R_{xy}(H)$ to a three-channel model in which two channels are n-type and the other is p-type:

$$\rho_{xx} = \frac{\sigma_{xx}}{\sigma_{xx}^2 + \sigma_{xy}^2} t \quad (1)$$

$$\rho_{xy} = \frac{\sigma_{xy}}{\sigma_{xx}^2 + \sigma_{xy}^2} t \quad (2)$$

$$\sigma_{xx} = \sum_{i=1}^3 \frac{n_i e \mu_i}{1 + (\mu_i \mu_0 H)^2} \quad (3)$$

$$\sigma_{xy} = \sum_{i=1}^3 \frac{n_i e \mu_i^2 \mu_0 H}{1 + (\mu_i \mu_0 H)^2} \quad (4)$$

where $\rho_{xx} = R_{xx} \frac{wt}{l}$ (thickness $t = 6$ nm, width $w = 100$ μm , length $l = 300$ μm) and $\rho_{xy} = R_{xy} t$ denote the longitudinal and Hall resistivities, respectively; σ_{xx} and σ_{xy} are the 2D longitudinal and Hall sheet conductivities, respectively; n_i is the 2D carrier density (positive); e and μ_i denote the carrier charge and mobility, respectively (negative for electrons and positive for holes); and $\mu_0 = 4\pi \times 10^{-7} \text{ H m}^{-1}$ is the nominal free-space permeability constant.

It is evident that the two fits in Figure 3b match the data extremely well. On the other hand, the fitting turns out to be poor if one considers either a two-channel model, or a three-channel model with one n-type and the other two p-type (see Figure S3 and Table S2, Supporting Information). These results, taken together, indicate that the three-channel model adopted here can accurately describe the electrical transport properties of these α -Sn films. Note that the fitting shown in Figure 3b is for a field range from -40 kOe to 40 kOe, not for the entire field range, because Equations (3) and (4) are valid

for weak fields only. Fits for different field ranges are presented in Section S5, Supporting Information.

The table in Figure 3c gives parameters from the fits in Figure 3b, along with sheet resistance $R_{s,i} = (n_i e \mu_i)^{-1}$ values, shown for reference. The carriers in the first two channels have relatively high density and low mobility. They can be assigned to holes and electrons activated thermally for the bulk states. As reported previously,^[26,27] due to the band crossing at the Fermi level (see Figure 1a), TDS materials can undergo thermal activation in which electrons in the valence band (green lines) below the Dirac points can be thermally activated to the conduction band (blue lines) above the Dirac points. These carriers can also be attributed to indirect inter-band thermal transitions in the α -Sn film, as discussed previously.^[30]

The third channel can be assigned to the topological surface states (TSS). There are three main reasons for this. (1) The carriers are n-type, which agrees with the fact that the Dirac point of the TSS is below the Fermi level [see Figure 1a].^[18,19,20] An analysis based on the Figure 3c parameters indicates that the Dirac point of the TSS is about 0.14 eV below the Fermi level (see Section S5, Supporting Information). This is roughly consistent with previous ARPES measurement results.^[18,24,25] (2) The carrier mobility of the third channel is relatively high. This is expected. In contrast with bulk states or trivial surface states, the TSS do not undergo backscattering. In the case that the surface states are trivial or non-topological, one would expect a low mobility because the states could be localized by disorder or defects on the film surface. This is plausible, in that the α -Sn film consists of nanoscale grains [see Figure 2c and Ref. [29]]. (3) Finally, the presence of the TSS in sputtered α -Sn thin films has been recently confirmed from a comprehensive ferromagnetic resonance study on a series of Sn/ferromagnet layered structures.^[34]

Two other important results are evident from the table in Figure 3c. (1) The carrier density is larger for the first channel than for the second channel. This difference indicates that the net carrier density of the bulk states is p-type, and the Fermi level is therefore below the bulk Dirac point (see Section S5, Supporting Information), rather than exactly cutting it as in the schematic diagram in Figure 1a. (2) The sheet resistance data indicate that the bulk states account for $\approx 68\%$ of the conductivity of the α -Sn film, while the TSS account for about 32%. Both components are important, but the bulk states dominate.

Figure 3d,e presents the temperature (T)-dependent R_{xx} or G_{xx} data that further confirm the TDS nature of the α -Sn films. In Figure 3d, the solid circles show the R_{xx} data, while the red curve is a fit to

$$\frac{1}{R_{xx}(T)} = \frac{1}{R_{\text{semi}}(T)} + \frac{1}{R_{\text{metal}}(T)} \quad (5)$$

$$R_{\text{semi}}(T) = R_{\infty} e^{\frac{E_g}{k_B T}} \quad (6)$$

$$\frac{1}{R_{\text{metal}}(T) - R_0} = \frac{1}{C_1 T} + \frac{1}{C_2 T^5} \quad (7)$$

The term R_{semi} denotes the semiconducting-like resistance associated with the thermal activation described above. Equation (6) follows the Arrhenius model.^[30] The term R_{metal}

describes the metallic-like resistance due to the scattering of electrons with phonons. Equation (7) follows the Bloch–Grüneisen model.^[30] Note that in Equation (6), R_∞ denotes the resistances at the high T limit, E_g represents the activation energy, and k_B is the Boltzmann constant; In Equation (7), R_0 is the resistance at $T = 0$ K due to electron-defect scattering, and C_1 and C_2 are constants related to the prevalence of electron-phonon interactions in the metallic states and the dimensions of the Hall bar structure. In order to better present the two contributions in Equation (5), Figure 3e gives the G_{xx} data, the fitted G_{xx} values, and the two components of the fitted values.

Figure 3d,e shows two significant results. (1) The $R_{xx}(T)$ curve shows a peak response, with a semiconducting-like behavior in the high T region while a metallic-like behavior in the low T region. This is consistent with the $R_{xx}(T)$ responses observed previously in other TDS thin films.^[26,27,30] (2) The experimental data can be fitted very well over the entire T range; the fitting yields $E_g = 68 \pm 3$ meV, which is comparable to the 81 meV value reported previously for an MBE-grown α -Sn thin film.^[30] These two observations together evidently support the above interpretation of the thermal activation process.

Several notes should be made about the data in Figure 3d,e. (1) The metallic component shown by the orange curve in Figure 3e includes contributions from both the bulk and the TSS, and the fitting analysis does not allow for the quantitative separation of the two contributions. (2) The other parameters from the fitting include $R_\infty = 655 \Omega$, $R_0 = 6.45 \text{ k}\Omega$, $C_1 = 20 \Omega \text{ K}^{-1}$, and $C_2 = 1.77 \times 10^{-5} \Omega \text{ K}^{-5}$. (3) The fitting analysis was also carried out with the T^{-5} term in Equation (7) replaced by a T^{-4} term, as in ref. [30]. The fit obtained is very similar to that shown in Figure 3d,e, except that a slightly higher E_g value (71 ± 3 meV) yielded. (4) R_{xx} at $T = 0$ in Figure 3d is not the same as R_{xx} at $H = 0$ in Figure 3b. Possible reasons for this include the differences in the α -Sn film thicknesses and the capping layers.

Figure 4 shows the main data on SOT-induced magnetization switching. Figure 4a shows the basic experimental configuration, with a picture of the switching device on the left and a diagram of the layered structure on the right. Figure 4b,c presents the magneto-optical Kerr effect (MOKE) data for field- and current-induced switching, respectively, both measured at room temperature.

As shown in Figure 4a, the core of the switching device is a $30 \mu\text{m} \times 15 \mu\text{m}$ rectangle made of an α -Sn(6 nm)/Ag(2 nm)/CoFeB(2 nm) trilayer structure. A 6 nm-thick α -Sn film was

used for three reasons. (1) Thicker films may have the β phase, not the α phase, as the dominant phase, as shown in Figure 2a; β -Sn films do have SOC in the bulk, but it is weak and no stronger than that in Ag.^[34] (2) In thinner films there may exist a quantum confinement effect that can turn the films into TI materials or quantum spin Hall insulators.^[35,36] (3) The transport properties of the 6 nm α -Sn film are already known, as presented in Figure 3.

The CoFeB layer in the structure is a ferromagnetic amorphous alloy. The easy axis in the CoFeB film is along the rectangle length directions (the y axis), as discussed in Section S9, Supporting Information. This facilitates the switching of the magnetization (\mathbf{M}) between the $\pm y$ directions.

The Ag layer works as a spacer to physically separate the active films. Previous work has shown that in a TI/ferromagnet bilayered structure, the TSS can be modified or even suppressed by the magnetic ordering in the ferromagnet.^[37,38,39] Recent experiments have demonstrated that this is actually the case in α -Sn/ferromagnet bilayers.^[25] The data also showed that an ultrathin Ag spacer could protect the TSS in the α -Sn film. Silver was chosen as a spacer for two main reasons. First, it has a long spin diffusion length (≈ 700 nm) and a small spin Hall angle (0.0068)^[40] and can therefore enable efficient transfer of spin from the α -Sn film to the CoFeB film. Second, the proximity-induced magnetic moment in Ag is only $0.0136\mu_B$ per atom,^[41] or smaller,^[42] one order of magnitude below that of Pt ($0.42\mu_B$)^[43] or Pd ($0.41\mu_B$).^[44] If the moment induced in Ag is large, it could modify or suppress the TSS in the α -Sn film.^[37,38,39] The Ag spacer thickness was chosen to be 2 nm in this work, mainly because the same thickness had been used for the α -Sn/Ag/Fe and α -Sn/Ag/NiFe heterostructures in previous studies.^[25,34]

The data in Figure 4b indicate that the CoFeB element can be switched with a modest magnetic field of about 80 Oe. The data in Figure 4c show that the same switching can be achieved by a current, in the absence of an external field. It is believed that this switching is induced by the spin current in the α -Sn film that is produced by the charge current along the x axis and has a spin polarization along the y axis [see Figure 1c]. The spin current exerts an anti-damping torque on \mathbf{M} , and the latter induces domain nucleation and drives domain walls to move in the CoFeB film. This gives rise to switching of \mathbf{M} between the $\pm y$ directions. Such switching through SOT-driven domain wall motion is the same as in previous SOT switching in TI- and

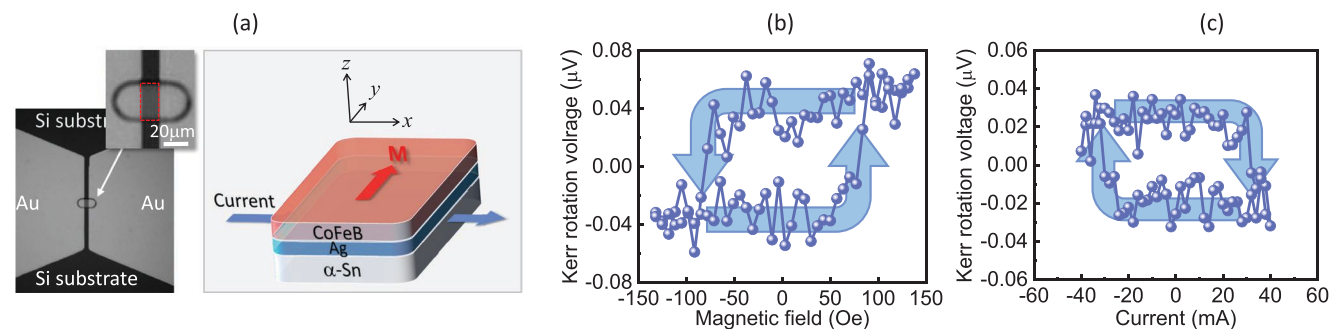


Figure 4. Magnetization switching in a Si/ α -Sn(6 nm)/Ag(2 nm)/CoFeB(2 nm) structure. a) Experimental configuration. b) Field-induced switching measured by a magneto-optical Kerr effect (MOKE) technique. c) Field-free, current-induced switching measured by the MOKE technique.

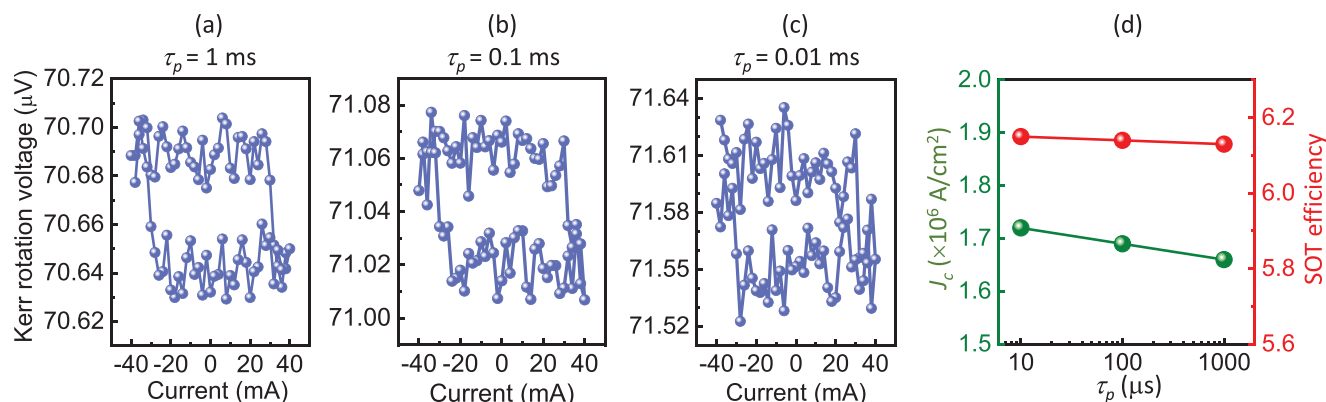


Figure 5. Effects of current pulse duration (τ_p) on switching in a Si/ α -Sn(6 nm)/Ag(2 nm)/CoFeB(2 nm) structure. a,b,c) The switching responses for three different τ_p , as indicated. d) The switching current density (J_c) and SOT efficiency (θ) as a function of τ_p .

Weyl-semimetal-based structures.^[8,14] It shares the same geometry as the so-called type- γ switching.^[45] More details about the switching processes are given in Section S14, Supporting Information. The data in Figure 4c were obtained with current pulse widths (τ_p) of 0.1 ms. The switching currents were 31.1 mA, which corresponds to a current density (J_c) of 1.69×10^6 A cm⁻² in the α -Sn film.

Several additional remarks are in order. First, prior to the data collection for Figure 4b,c), an external field was applied to saturate \mathbf{M} in the CoFeB film along the $+\gamma$ direction. Second, the two hysteresis loops in Figure 4b,c are shown to evolve in opposite senses. This is solely due to the definition of the sign of the charge current; a flip in the current sign would lead to two loops with the same evolution. Third, the overall change of the MOKE voltage in Figure 4c is slightly smaller than that in Figure 4b. There are two possible reasons for this difference. (1) The current-induced switching may not be as complete as the field-induced switching due to the use of a modest charge current. (2) There may be a difference in the position of the MOKE laser beam relative to the device center during the measurements that could cause a difference in the intensity of the MOKE signals. Finally, the MOKE loops in Figure 4b,c are quite noisy, due presumably to the use of extremely thin (2 nm) CoFeB films. Averaging of signals from multiple measurements could be used to improve the signal-to-noise ratio. Nevertheless, the switching response is in clear evidence.

The field-free, room-temperature, current-induced switching shown in Figure 4 is very intriguing. In order to be sure the process is indeed SOT-induced magnetization switching, it is important to consider other options such as processes arising from (1) the Oersted field produced by the current, (2) current-caused Joule heating, or (3) a SOT process due to the bulk of the α -Sn film. These alternatives are considered below.

Consider option (1), Oersted field switching. The switching current cited above corresponds to an Oersted field of ≈ 4.6 Oe. This is significantly smaller than the switching field shown in Figure 4b. Thus, one cannot attribute the current switching to the Oersted field. One caveat may apply, however. Some of the imperfections at the edges or corners of the CoFeB element may comprise optimum locations for domain nucleation. It is possible that the current-produced Oersted fields are strong enough to trigger domain nucleation at those locations.

One reverse caveat also may apply, however. One would need a much larger Oersted field (about 80 Oe) to move the domain walls across the entire CoFeB element to a sufficient degree to obtain switching.

Consider option (2), heating-associated switching. Figure 5 shows switching data for different pulse widths. One can see that a decrease in the pulse width τ_p gives rise to a slightly noisier loop, but no notable changes in the loop width. Specifically, as τ_p is reduced by two orders of magnitudes, the switching current J_c increases only by about 3.6%. These results are discussed in detail in Section S13, Supporting Information. It is clear that the switching responses shown here cannot be attributed to the heating effects produced by the current.

Further checks were made based on additional data on two control samples, one with no α -Sn layer and one with no Ag layer. Comparison data are shown in Figure 6. Specifically, the data in a,b,c) present the MOKE signals for α -Sn(6 nm)/Ag(2 nm)/CoFeB(2 nm), Ag(2 nm)/CoFeB(2 nm), and α -Sn(6 nm)/CoFeB(2 nm), respectively. The control samples were prepared using the same substrates, targets, and sputtering conditions. It is evident that no switching responses are observed in Figure 6b,c), even with larger currents. It is abundantly clear that the switching results shown in Figure 4 cannot be attributed to the current-produced Oersted field or heating.

Further, the absence of a switching response in the α -Sn/CoFeB control sample with no intermediate Ag spacer indicates that the SOT from the bulk of the α -Sn film alone is not sufficient to switch the CoFeB layer. This result is consistent with recent experimental work that showed that the SOC in the bulk of sputtered α -Sn films is no stronger than that in Ag.^[34] Note that there are no TSS at the α -Sn/CoFeB interface, due to the reason mentioned above. Any SOT effects, if present in the structure, would be mostly due to the bulk of the α -Sn film. As such, option (3) can be ruled out. Additionally, the absence of a switching response in the α -Sn/CoFeB sample also suggests that band bending-associated Rashba effects, if present at the α -Sn surfaces, are too weak to induce switching. This is discussed in Section S17, Supporting Information.

In summary, the experimental data presented in Figures 5 and 6 evidently show that the demonstrated magnetization switching is induced by the SOT associated with the TSS in the α -Sn film. It is not due to the current-produced Oersted field,

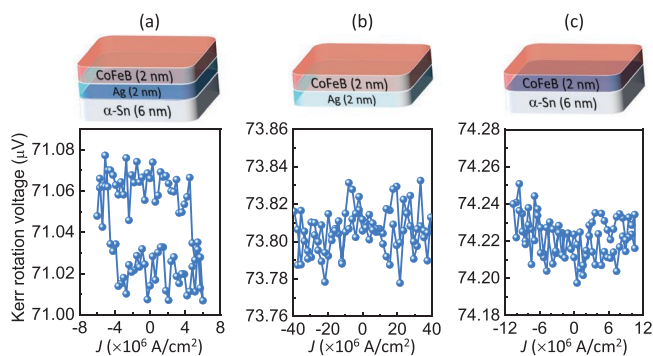


Figure 6. Comparison of MOKE voltage versus current responses in three different structures.

Joule heating, an SOT associated with the bulk states in the α -Sn, or interfacial Rashba effects.

The above results, considered as a whole, demonstrate that the current switching in the α -Sn/Ag/CoFeB sample is mostly associated with the TSS in the structure. This suggests that TSS in TDS α -Sn can be utilized to manipulate magnets, just as TSS in TI materials. In order to compare the efficiencies of TDS α -Sn with TI materials as well as heavy metals in terms of SOT production, one can define a dimensionless charge-to-spin conversion efficiency as

$$\theta = \frac{J_s}{J_c} \quad (8)$$

where J_s and J_c denote the nominal spin current density and the charge current density, respectively. This SOT efficiency can be easily estimated from the switching current measured experimentally.^[8] It corresponds to the spin Hall angle of a material in which the same charge current density as in the α -Sn film could produce the same spin current density.

The red points in Figure 5d represent the estimated efficiency θ values. The details about the θ evaluation are provided in Section S14, Supporting Information. The data in Figure 5d show that as the current duration is reduced by two orders of magnitude, θ remains almost unchanged as expected, being around 6.1. This value is comparable to that in TI thin films and is one order of magnitude higher than that in heavy metals (see Table S3, Supporting Information); previous work showed $\theta = 1.7$ in $\text{Bi}_x\text{Se}_{1-x}$ at room temperature,^[8] $\theta = 2.0$ – 3.5 in Bi_2Se_3 at 4.2 K,^[46] and $\theta = 0.15$ in Ta at room temperature.^[3]

The parameter θ defined by Equation (8) enables a straightforward comparison of the efficiency in this work with the efficiencies reported previously in the interpretation of charge-to-spin conversion in TIs and heavy metals, but strictly speaking it is inappropriate to use θ to characterize the efficiency in this work as the switching is mostly associated with the 2D TSS, rather than the bulk states in the α -Sn. Instead, one can define a 2D efficiency as^[47,48]

$$q = \frac{J_s}{j_c} \quad (9)$$

where J_s is the 3D spin current density as in Equation (8), while j_c is the 2D surface current density for the TSS. With R_s in the table in Figure 3c, one obtains $q \approx 6.3 \text{ nm}^{-1}$ for the TSS in the α -Sn (see Section S15, Supporting Information). This value is comparable to the previously reported value (1.0 nm^{-1}) for Sb_2Te_3 .^[47] This result further shows that the SOT efficiency in the α -Sn in this work is comparable to that in TI thin films.

With the above-determined SOT efficiency, it is also possible to estimate the power consumption for the SOT switching in the α -Sn/Ag/CoFeB structure. Following the analysis procedures in ref. [49], one finds that the power needed for switching in the α -Sn/Ag/CoFeB structure is two or three orders of magnitude lower than that in heavy-metal-based SOT switching devices, as shown in Section S16, Supporting Information. This result further demonstrates the merit of TDS α -Sn for energy-efficient SOT spintronic device applications.

Five final remarks are as follows.

1. This work demonstrates α -Sn TSS-induced field-free room-temperature switching of a ferromagnet with in-plane magnetization. Future studies using ferromagnets with perpendicular anisotropy are important from the perspectives of high-density memory and logic applications. Note that the SOT memory concept is very attractive currently as it allows for low-current switching and also enables the separation of the writing and reading channels.
2. The switching in this work is realized through domain nucleation and domain wall motion, as in previous SOT switching in TI- and Weyl-semimetal-based structures.^[8,14] The reason for this is that the size of the switching element is much larger than the domain wall width (280 nm; see Section S12, Supporting Information). Though this work is of great interest for racetrack memory applications,^[50] future work is also of great interest to demonstrate the switching of a nanoscale, single-domain magnetic island by an SOT from a neighboring α -Sn layer. The switching in such an island will be achieved through magnetization rotation, which will be induced by the SOT in the same manner as the domain nucleation and the dynamics associated with the domain wall motion are driven by the SOT in this work. Note that switching in a nanoscale ferromagnetic island cannot be measured by the conventional MOKE technique, but it can be detected electrically via the differential planar Hall effect if \mathbf{M} is in-plane,^[51] or via the anomalous Hall effect if \mathbf{M} is out-of-plane.
3. Future work is also of great interest that makes use of strain engineering to modify the band structure^[18,19,20] or voltage gating to tune the Fermi level in α -Sn, to examine the effects of the bulk states on the spin-momentum locking in the TSS, and also explore the possibilities of realizing α -Sn thin films with an even higher SOT efficiency. In the case of TI materials, it has been demonstrated experimentally that a decrease in the bulk conductivity could either largely enhance or suppress the spin-momentum locking of the TSS.^[47,52] Moreover, recent theoretical and experimental studies show that the introduction of graphene as an interlayer to a TI-based heterostructure can result in substantial enhancement in SOC and thereby give rise to strong Rashba–Edelstein effects in the structure.^[53,54] It would be very interesting in future

to explore the switching efficiency enhancement through the replacement of the Ag spacer in the α -Sn/Ag/CoFeB trilayer structures with graphene.

4. As mentioned above, the existence of the TSS in α -Sn thin films has been confirmed previously through ARPES measurements by a number of different research groups.^[18,23,24,25,30,36,55] Further, there has also been previous work that used spin-resolved ARPES measurements to confirm the spin-momentum locking of the TSS in α -Sn thin films.^[23,24] Though the transport and switching data presented above evidently indicates the presence of the TSS in the α -Sn films in this work, it is still worthy to use the ARPES technique to measure the TSS in the films in the future.
5. In addition to the TSS concerned in this work, TDS α -Sn should also host topological Fermi arc surface states;^[56] these states are expected to exist on surfaces parallel to the uniaxial tensile axis,^[19] namely, the four side surfaces of the α -Sn film in this work. It is interesting to study how to use such Fermi arc states for SOT switching in the future.

Experimental Section

The α -Sn thin films were grown on single-crystal (111) Si substrates by DC magnetron sputtering. The substrates were rinsed sequentially with acetone, isopropyl alcohol, and DI water before being loaded into the sputtering chamber. Prior to sputtering, the chamber had a base pressure of 2.0×10^{-8} Torr; substrate biasing was performed that included several cycles of Ar ion sputtering of the substrate surface and the post-annealing of the substrate at 250 °C. The Ar ion sputtering process was aimed at removing the thin oxidized layer on the top of the substrate, while the post-annealing process was taken to remove the moisture adherent on the substrate surface. After removing the oxidized layer and the surface moisture, the α -Sn deposition was then carried out at room temperature, at a rate of about 2 nm min⁻¹. The sputtering power was set to a low value of 15 W, in order to minimize the heating effect during the deposition. The layered heterostructures in this work were all grown in the same sputtering chamber without breaking the vacuum. The film thicknesses were determined through X-ray reflection and atomic force microscopy (AFM) measurements.

The measurements of the electrical transport properties of α -Sn thin films made use of a Hall bar device fabricated through photolithography and argon ion milling processes. The switching device was fabricated from a Si/Sn(6 nm)/Ag(2 nm)/CoFeB(2 nm) thin-film stack. The measurements of the magnetization switching were carried out with a longitudinal MOKE system.

More details about the materials and the methods are provided in the Supporting Information.

Supporting Information

Supporting Information is available from the Wiley Online Library or from the author.

Acknowledgements

J.D., C.L., and V.K. contributed equally to this work. This work was supported by the U.S. Department of Energy, Office of Science, Basic Energy Sciences (DE-SC0018994). The development and characterization of α -Sn thin film materials were supported by Western Digital. The magnetic hysteresis measurements, ferromagnetic resonance

measurements, and domain simulations of the CoFeB thin films were supported by the U.S. National Science Foundation (EFMA-1641989; ECCS-1915849). Work at NJU was supported by the National Natural Science Foundation of China (11734006; 11974165). Work at UW was supported by the U.S. National Science Foundation (DMR-1710512) and the U.S. Department of Energy, Office of Science, Basic Energy Sciences (DE-SC0020074; DE-SC0021281).

Conflict of Interest

The authors declare no conflict of interest.

Data Availability Statement

The data that support the findings of this study are available from the corresponding author upon reasonable request.

Keywords

ferromagnets, magnetization switching, spin-orbit torque, topological Dirac semimetals, topological quantum materials, topological surface states

Received: August 30, 2020

Published online:

- [1] I. M. Miron, G. Gaudin, S. Auffret, B. Rodmacq, A. Schuhl, S. Pizzini, J. Vogel, P. Gambardella, *Nat. Mater.* **2010**, 9, 230.
- [2] L. Liu, O. J. Lee, T. J. Gudmundsen, D. C. Ralph, R. A. Buhrman, *Phys. Rev. Lett.* **2012**, 109, 096602.
- [3] L. Liu, C.-F. Pai, Y. Li, H. W. Tseng, D. C. Ralph, R. A. Buhrman, *Science* **2012**, 336, 555.
- [4] S. Emori, U. Bauer, S.-M. Ahn, E. Martinez, G. S. D. Beach, *Nat. Mater.* **2013**, 12, 611.
- [5] Z. Duan, A. Smith, L. Yang, B. Youngblood, J. Lindner, V. E. Demidov, S. O. Demokritov, I. N. Krivorotov, *Nat. Commun.* **2014**, 5, 5616.
- [6] Y. Fan, P. Upadhyaya, X. Kou, M. Lang, S. Takei, Z. Wang, J. Tang, L. He, L.-T. Chang, M. Montazeri, G. Yu, W. Jiang, T. Nie, R. N. Schwartz, Y. Tserkovnyak, K. L. Wang, *Nat. Mater.* **2014**, 13, 699.
- [7] J. Han, A. Richardella, S. A. Siddiqui, J. Finley, N. Samarth, L. Liu, *Phys. Rev. Lett.* **2017**, 119, 077702.
- [8] Y. Wang, D. Zhu, Y. Wu, Y. Yang, J. Yu, R. Ramaswamy, R. Mishra, S. Shi, M. Elyasi, K.-L. Teo, Y. Wu, H. Yang, *Nat. Commun.* **2017**, 8, 1364.
- [9] K. Yasuda, A. Tsukazaki, R. Yoshimi, K. Kondou, K. S. Takahashi, Y. Otani, M. Kawasaki, Y. Tokura, *Phys. Rev. Lett.* **2017**, 119, 137204.
- [10] Y. Li, Q. Ma, S. X. Huang, C. L. Chien, *Sci. Adv.* **2018**, 4, eaap8294.
- [11] D. C. M, R. Grassi, J.-Y. Chen, M. Jamali, D. R. Hickey, D. Zhang, Z. Zhao, H. Li, P. Quarterman, Y. Lv, M. Li, A. Manchon, K. A. Mkhoyan, T. Low, J.-P. Wang, *Nat. Mater.* **2018**, 17, 800.
- [12] N. H. D. Khang, Y. Ueda, P. N. Hai, *Nat. Mater.* **2018**, 17, 808.
- [13] P. Li, J. Kally, S. S.-L. Zhang, T. Pillsbury, J. Ding, G. Csaba, J. Ding, J. S. Jiang, Y. Liu, R. Sinclair, C. Bi, A. DeMann, G. Rimal, W. Zhang, S. B. Field, W. W. J. Tang, O. G. Heinonen, V. Novosad, N. S. A. Hoffmann, M. Wu, *Sci. Adv.* **2019**, 5, eaaw3415.
- [14] S. Shi, S. Liang, Z. Zhu, K. Cai, S. D. Pollard, Y. Wang, J. Wang, Q. Wang, P. He, J. Yu, G. Eda, G. Liang, H. Yang, *Nanotechnol.* **2019**, 14, 945.

- [15] D. MacNeill, G. M. Stiehl, M. H. D. Guimaraes, R. A. Buhrman, J. Park, D. C. Ralph, *Nat. Phys.* **2016**, *13*, 300.
- [16] B. Zhao, B. Karpiak, D. Khokhriakov, A. Johansson, A. M. Hoque, X. Xu, Y. Jiang, I. Mertig, S. P. Dash, *Adv. Mater.* **2020**, *32*, 2000818.
- [17] B. Zhao, D. Khokhriakov, Y. Zhang, H. Fu, B. Karpiak, A. M. Hoque, X. Xu, Y. Jiang, B. Yan, S. P. Dash, *Phys. Rev. Res.* **2020**, *2*, 013286.
- [18] C.-Z. Xu, Y.-H. Chan, Y. Chen, P. Chen, X. Wang, C. Dejoie, M.-H. Wong, J. A. Hlevyack, H. Ryu, H.-Y. Kee, N. Tamura, M.-Y. Chou, Z. Hussain, S.-K. Mo, T.-C. Chiang, *Phys. Rev. Lett.* **2017**, *118*, 146402.
- [19] H. Huang, F. Liu, *Phys. Rev. B* **2017**, *95*, 201101(R).
- [20] D. Zhang, H. Wang, J. Ruan, G. Yao, H. Zhang, *Phys. Rev. B* **2018**, *97*, 195139.
- [21] S. C. Zhang, X. L. Qi, *Phys. Today* **2010**, *63*, 12.
- [22] Z. Zhu, Y. Cheng, U. Schwingenschlög, *Phys. Rev. B* **2012**, *85*, 235401.
- [23] A. Barfuss, L. Dudy, M. R. Scholz, H. Roth, P. Höpfner, C. Blumenstein, G. Landolt, J. H. Di, N. C. Plumb, M. Radovic, A. Bostwick, E. Rotenberg, A. Fleszar, G. Bihlmayer, D. Wortmann, G. Li, W. Hanke, R. Claessen, J. Schäfer, *Phys. Rev. Lett.* **2013**, *111*, 157205.
- [24] Y. Ohtsubo, P. L. Fèvre, F. Bertran, A. Taleb-Ibrahimi, *Phys. Rev. Lett.* **2013**, *111*, 216401.
- [25] J.-C. Rojas-Sánchez, S. Oyarzún, Y. Fu, A. Marty, C. Vergnaud, S. Gambarelli, L. Vila, M. Jamet, Y. Ohtsubo, A. Taleb-Ibrahimi, P. Le Fèvre, F. Bertran, N. Reyren, J.-M. George, A. Fert, *Phys. Rev. Lett.* **2016**, *116*, 096602.
- [26] C.-Z. Li, L.-X. Wang, H. Liu, J. Wang, Z.-M. Liao, D.-P. Yu, *Nat. Commun.* **2015**, *6*, 10137.
- [27] H. Li, H. He, H.-Z. Lu, H. Zhang, H. Liu, R. Ma, Z. Fan, S.-Q. Shen, J. Wang, *Nat. Commun.* **2016**, *7*, 10301.
- [28] Y. Zhang, C. Wang, L. Yu, G. Liu, A. Liang, J. Huang, S. Nie, X. Sun, Y. Zhang, B. Shen, J. Liu, H. Weng, L. Zhao, G. Chen, X. Jia, C. Hu, Y. Ding, W. Zhao, Q. Gao, C. Li, S. He, L. Zhao, F. Zhang, S. Zhang, F. Yang, Z. Wang, Q. Peng, X. Dai, Z. Fang, Z. Xu, et al., *Nat. Commun.* **2017**, *8*, 15512.
- [29] I. Madarevic, U. Thupakula, G. Lippertz, N. Claessens, P.-C. Lin, H. Bana, S. Gonzalez, G. D. Santo, L. Petaccia, M. N. Nair, L. M. C. Pereira, C. V. Haesendonck, M. J. Van Bael, *APL Mater.* **2020**, *8*, 031114(R).
- [30] O. Vail, P. Taylor, P. Folkes, B. Nichols, B. Haidet, K. Mukherjee, G. de Coster, *Phys. Status Solidi B* **2020**, *257*, 1800513.
- [31] T. Liang, Q. Gibson, M. N. Ali, M. Liu, R. J. Cava, N. P. Ong, *Nat. Mater.* **2015**, *14*, 280.
- [32] N. Bansal, Y. S. Kim, M. Brahlek, E. Edrey, S. Oh, *Phys. Rev. Lett.* **2012**, *109*, 116804.
- [33] Q. Barbedienne, J. Varignon, N. Reyren, A. Marty, C. Vergnaud, M. Jamet, C. G.-Carbonell, A. Lemaître, P. L. Fèvre, F. Bertran, A. T.-Ibrahimi, H. Jaffrès, J.-M. George, A. Fert, *Phys. Rev. B* **2018**, *98*, 195445.
- [34] J. Ding, C. Liu, Y. Zhang, V. Kalappattil, R. Yu, U. Erugu, J. Tang, H. Ding, H. Chen, M. Wu, *Adv. Funct. Mater.* **2021**, *31*, 2008411.
- [35] Y. Xu, B. Yan, H.-J. Zhang, J. Wang, G. Xu, P. Tang, W. Duan, S.-C. Zhang, *Phys. Rev. Lett.* **2013**, *111*, 136804.
- [36] V. A. Rogalev, F. Reis, F. Adler, M. Bauernfeind, J. Erhardt, A. Kowalewski, M. R. Scholz, L. Dudy, L. B. Duffy, T. Hesjedal, M. Hoesch, G. Bihlmayer, J. Schäfer, R. Claessen, *Phys. Rev. B* **2019**, *100*, 245144.
- [37] L. A. Wray, S.-Y. Xu, Y. Xia, D. Hsieh, A. V. Fedorov, Y. S. Hor, R. J. Cava, A. Bansil, H. Lin, M. Z. Hasan, *Nat. Phys.* **2011**, *7*, 32.
- [38] J. Zhang, J. P. Velev, X. Dang, E. Y. Tsymlal, *Phys. Rev. B* **2016**, *94*, 014435.
- [39] J. M. Marmolejo-Tejada, K. Dolui, P. Lazic, P.-H. Chang, S. Smidstrup, D. Stradi, K. Stokbro, B. K. Nikolic, *Nano Lett.* **2017**, *17*, 5626.
- [40] H. L. Wang, C. H. Du, Y. Pu, R. Adur, P. C. Hammel, F. Y. Yang, *Phys. Rev. Lett.* **2014**, *112*, 197201.
- [41] N. Jaouen, F. Wilhelm, A. Rogalev, J. Goulon, L. Ortega, J. M. Tonnerre, B. Rodmacq, A. Yaresko, *J. Phys.: Condens. Matter* **2008**, *20*, 095005.
- [42] N. Jaouen, F. Wilhelm, A. Rogalev, J. M. Tonnerre, T. K. Johal, G. van der Laan, *IEEE Trans. Magn.* **2005**, *41*, 3334.
- [43] A. Moskalitsova, J. Krieff, D. Graulich, T. Matalla-Wagner, T. Kuschel, *AIP Adv.* **2020**, *10*, 015154.
- [44] J. Vogel, A. Fontaine, V. Cros, F. Petroff, J. P. Kappler, G. Krill, A. Rogalev, J. Goulon, *J. Magn. Magn. Mater.* **1997**, *165*, 96.
- [45] S. Fukami, T. Anekawa, C. Zhang, H. Ohno, *Nat. Nanotechnol.* **2016**, *11*, 621.
- [46] A. R. Mellnik, J. S. Lee, A. Richardella, J. L. Grab, P. J. Mintun, M. H. Fischer, A. Vaezi, A. Manchon, E.-A. Kim, N. Samarth, D. C. Ralph, *Nature* **2014**, *511*, 449.
- [47] K. Kondou, R. Yoshimi, A. Tsukazaki, Y. Fukuma, J. Matsuno, K. S. Takahashi, M. Kawasaki, Y. Tokura, Y. Otani, *Nat. Phys.* **2016**, *12*, 1027.
- [48] J.-C. Rojas-Sánchez, A. Fert, *Phys. Rev. Appl.* **2019**, *11*, 054049.
- [49] L. Zhu, R. A. Buhrman, *Phys. Rev. Appl.* **2019**, *12*, 051002.
- [50] S. Parkin, S. H. Yang, *Nat. Nanotechnol.* **2015**, *10*, 195.
- [51] G. Mihajlović, O. Mosendz, L. Wan, N. Smith, Y. Choi, Y. Wang, J. A. Katine, *Appl. Phys. Lett.* **2016**, *109*, 192404.
- [52] A. Dankert, P. Bhaskar, D. Khokhriakov, I. H. Rodrigues, B. Karpiak, M. V. Kamalakar, S. Charpentier, I. Garate, S. P. Dash, *Phys. Rev. B* **2018**, *97*, 125414.
- [53] M. Rodriguez-Vega, G. Schwiete, J. Sinova, E. Rossi, *Phys. Rev. B* **2017**, *96*, 235419.
- [54] D. Khokhriakov, A. M. Hoque, B. Karpiak, S. P. Dash, *Nat. Commun.* **2020**, *11*, 3657.
- [55] A. Rogalev, T. Rauch, M. R. Scholz, F. Reis, L. Dudy, A. Fleszar, M.-A. Husanu, V. N. Strocov, J. Henk, I. Mertig, J. Schäfer, R. Claessen, *Phys. Rev. B* **2017**, *95*, 161117(R).
- [56] S.-Y. Xu, C. Liu, S. K. Kushwaha, R. Sankar, J. W. Krizan, I. Belopolski, M. Neupane, G. Bian, N. Alidoust, T.-R. Chang, H.-T. Jeng, C.-Y. Huang, W.-F. Tsai, H. Lin, P. P. Shibayev, F.-C. Chou, R. J. Cava, M. Z. Hasan, *Science* **2015**, *347*, 294.